Available online at www.sciencedirect.com

ScienceDirect

Ceramics International 40 (2014) 14881–14889

CERAMICS INTERNATIONAL

www.elsevier.com/locate/ceramint

In situ formation of Fe–NbC/C composite powders from solution-derived precursors by a gas reduction–carburization process

María Belén Gilliard, Beatriz Teresita Pierini, Silvia Alejandra Alconchel*

Departamento de Química, Facultad de Ingeniería Química, Universidad Nacional del Litoral, Santiago del Estero 2829, S3000AOM Santa Fe, Argentina

Received 6 May 2013; received in revised form 16 June 2014; accepted 16 June 2014
Available online 21 June 2014

Abstract

The *in situ* formation of Fe–NbC/C composite powders was studied using solution-derived precursors and a gas reduction–carburization reaction at 1223 K. The effect of different CH_4/H_2/Ar gas mixtures or a polymer (polyvinyl alcohol – PVA) combined with sucrose as carbon sources was analyzed. The results obtained were discussed in relation to the reduction–carburization sequence, microstructure and oxidation behavior of the composite powders. When the carbon was supplied by the gas phase (CH_4), the reaction mechanism proceeded *via* $FeNb_2O_6 \rightarrow Fe + NbO_2 \rightarrow Fe + NbC$. However, if the carbon was generated in the solid phase, from PVA–sucrose pyrolysis, the transformation to the compound powder was achieved faster by means of a carbothermal reduction reaction. The type of free carbon was characterized by a high degree of disorder and defined not only the powder microstructure but also the crystallite size of the reinforcement phase (NbC) and certain behavior features during oxidation. The carbon generated by PVA–sucrose pyrolysis (70 wt%) was the most adequate one to obtain a sponge-type morphology with nanocrystalline NbC (12 nm) and to protect the Fe particles from oxidation. Even so, all the composite powders prepared remained stable in air up to about 600 K.

Keywords: A. Powders: chemical preparation; B. Electron microscopy; C. Oxidation; D. Carbides

1. Introduction

Composites with iron and ceramic particle reinforcements, such as NbC or TaC, play a key role in the production of relatively inexpensive and more environment-friendly wear-resistant materials. They are usually produced by powder metallurgy (P/M route, including high-energy milling-HEM, compacting and sintering) from iron and carbide powders prepared separately [1–3]. The typical advantages of this P/M route, referred to as *ex situ* processing, are raw-material savings and low energy costs. However, the composites thus obtained generally suffer from the problem of contaminated matrix–reinforcement interfaces with a weak bonding.

From this viewpoint, the techniques involving the *in situ* generation of the reinforcement phase have emerged as a preferred synthesis route for these materials. *In situ* techniques involve a chemical reaction resulting in the formation of a very fine and thermodinamically stable ceramic phase within a metal matrix. Consequently, the reinforcement surfaces are likely to be free from gas absorption, oxidation or other detrimental types of surface reaction contamination. Therefore, the interface between the matrix and the reinforcement bond tends to be stronger. Some of these technologies applied to synthesize Fe-NbC/TaC composites include the carbothermal reduction of columbite ores at 1673–1873 K [4,5], self-propagating high temperature (SHS) synthesis [6], infiltration casting process combined with heat treatment at 1445 K [7] and mechanical alloying of dry powder mixtures (FeNb + C, heated at 1073 K; Fe + Nb + C, followed by sintering at 1573 K) [8–10] or powder mixtures in organic media (Fe + Nb + toluene, including a method of magnetic pulse compaction) [11]. In most cases, while high-temperature ensures a fast, complete reaction, it also causes the coarsening of the carbide grains. For example, the particulate-reinforced composite produced by SHS cannot be directly used as structural material

*Corresponding author. Tel./fax: +54 342 4571164.
E-mail addresses: belen_gilliard@hotmail.com (M.B. Gilliard), bpierini@fiq.unl.edu.ar (B.T. Pierini), salco@fiq.unl.edu.ar (S.A. Alconchel).

http://dx.doi.org/10.1016/j.ceramint.2014.06.083
0272-8842/

because of its porosity and looseness, making the intrinsic porosity in the reaction process difficult to handle.

It is well known that the reduction of the carbide size causes a significant improvement of the mechanical properties. The toughness of ceramics could be considerably increased by reducing grain size without sacrificing hardness. In this sense, alternative synthesis procedures of nanocrystalline composite powders, such as a gas reduction–carburization [12] and polymer-derived precursors [13], could be useful in assisting composite homogenization and densification and, therefore, in tailoring the final properties of the composite.

The present work proposes an alternative route to synthesize Fe–NbC/C composite powders, which combines the advantages of solution-derived precursors with a gas reduction–carburization reaction. This article pays particular attention to the effect of CH_4/H_2/Ar gas mixtures or a polymer (polyvinyl alcohol – PVA) as carbon sources, on the *in situ* formation of the composite. Additionally, the microstructure and oxidation behavior of the composite powders are investigated and discussed in relation to the carbon supply from the solid or gas phase.

2. Materials and methods

2.1. Preparation

The synthesis of Fe–NbC/C composite powders was performed in four sequential steps, as shown in Fig. 1. The materials used as reagents were $Fe(NO_3)_3 \cdot 9H_2O$ (Merck, 99.9%) and $Nb(NH_4)[NbO(C_2O_4)_2(H_2O)_2](H_2O)_n$ (CBMM, Companhia Brasileira de Metalurgia e Mineração). Starting Fe (0.1 mol L^{-1}) or Nb (0.1 mol L^{-1}) containing solutions were prepared by dissolving their respective salts in distilled water and analyzed by complexometric and gravimetric analysis, respectively. $FeC_2O_4 \cdot 2H_2O$ and the $Fe_2(C_2O_4)_3$ aqueous solution were prepared and analyzed as reference 14 (step 1: individual solutions). Then, they were combined to obtain Fe:Nb = 1:1 source solutions with and without NO_3^- ions. The mixed-metal solution with nitrates was stable only in the presence of oxalic acid necessary to form an iron-oxalate complex (step 2: mixed-metal solutions). This solution was hydrolyzed by adding NH_3 2 mol L^{-1} up to pH = 10. The precipitate formed was filtered, washed and dried at 353 K for 24 h. On the other hand, the mixed-metal solution without nitrates was evaporated to dryness using a Büchi R-124 Rotavap at 333 K or a stirring hot plate at ~353 K. In the latter case, the mixed-metal solution was prepared by adding polyvinyl alcohol (Merck, PVA 72,000) 1 mol L^{-1} and sucrose 2 mol L^{-1} in the M:PVA = 2:1 (M: total metals) and sucrose:PVA = 4:1 M relations. In this way, dried solid precursors were obtained as amorphous (X-ray diffraction) loose powders, being brown, green or black according to the composition and experimental set-up preparation conditions (step 3: precursors).

Finally, the precursors were reduced–carburized by temperature-programmed reaction (TPRe) in different CH_4/H_2/Ar mixtures (0/4/96 vol%, 16/4/80 vol% and 4/16/80 vol%, > 99.99% purity). The TPRe experiments were performed using an Ohkura TP2002S analyzer equipped with a thermal conductivity detector (TCD). Between 150 and 200 mg of each precursor were loaded into an 8 mm (o.d.) quartz tube stuffed with quartz wool at the bottom to hold the powders. The powders were heated at 10 K min^{-1} up to 1223 K during variable times and, then, they were cooled by quenching at room temperature. This cooling process to room temperature was performed in the reactor under flowing gas-mixture 50 cm^3 min^{-1} (step 4: composite powders).

2.2. Characterization

The structure of precursors and composite powders was examined at room temperature by X-ray diffraction (XRD). Routine patterns were obtained from a Shimadzu XD-D1 automated diffractometer using graphite-monochromated Cu K_α

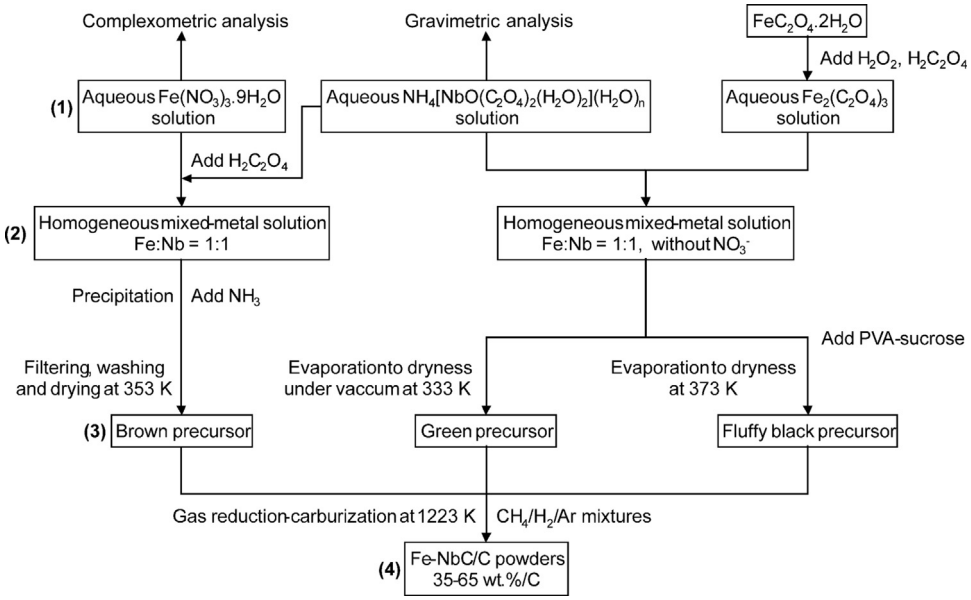

Fig. 1. Synthesis scheme for Fe–NbC/C composite powders.

radiation (30 kV, 40 mA). The data were collected with a scanning rate of $1^\circ\,min^{-1}$ over the 10–80° 2θ angular range with a collection time of 1 s. The Scherrer formula was used for the determination of the Fe and NbC crystallite size from the XRD pattern. The evaluation was performed from the highest intensity low angle Bragg reflections for each phase, Fe (110) and NbC (111), after instrumental line broadening correction.

The carbon content of composite powders was evaluated by standard combustion analysis (Carlo Erba EA 1108); N_2 and CO_2 were separated in a chromatographic column, and measured using a thermal conductivity detector. Besides, laser Raman spectroscopy (LRS) was used to monitor the type of carbon present in the samples. These spectra were measured at room temperature in a right-angle scattering geometry on powder samples in the spectral range 1050–1750 cm^{-1} by a Jasco TRS-600-SZ-P multichannel spectrometer. The 514.5 nm Ar^+-laser with about 80 mW incident power at the sample surface was used. The scanning time was 120 s and the spectral resolution in all the experiments was of about 4 cm^{-1}.

The microstructure of composite powders was examined by scanning electron microscopy together with X-ray microanalysis (SEM-EDX). A JEOL JSM-35C scanning electron microscope with an energy dispersive spectrometer was used at an accelerating voltage of 20 kV. The powders were dispersed on metallic or graphite sample holders and were covered with a thin film of gold only for secondary electron images.

The oxidation behavior of composite powders was studied by thermogravimetric and differential thermal analysis (TGA/DTA). The thermograms and simultaneous differential thermal profiles were obtained using a Mettler Toledo TGA/SDTA851e system. The samples were heated in air at 10 K min^{-1} up to 1223 K.

3. Results and discussion

3.1. Formation of Fe–NbC/C composite powders

As described in the experimental section, the gas reduction–carburization of the precursors was monitored by the TCD signal of a thermal analyzer. Fig. 2 shows the typical TPRe profiles for each precursor in different $CH_4/H_2/Ar$ gaseous mixtures. It should be first noticed that a return of the signal to the base line, which indicates no difference in composition between the gases going in and out of the reactor, marks the end of the reaction. (In some cases instrumental drift causes the signal to deviate from the base line at the end of the reaction.) In carburizations with $CH_4/H_2/Ar$ mixtures, the TCD signal obtained is complex. A positive signal results from a consumption of gases (decrease in thermal conductivity) and is indicative of the reduction of the precursor. A negative signal is due to the production of gases (increase in thermal conductivity) and is indicative of the carburization of the material. At times, both reduction and carburization processes occur simultaneously so that there can be a partial cancellation in the TCD signal.

In our case, when comparing the TPRe profiles taken in H_2/Ar (dotted line) and $CH_4/H_2/Ar$ (dashed and solid lines) for the brown precipitated precursor (Fig. 2a), it can be inferred that the positive signals ($t < 3720$ s, $T < 910$ K) correspond to a reduction process whereas the negative signals ($t > 4600$ s, $T > 1050$ K) are indicative of the additional interaction with methane and, hence, of the carburization of the solid. The composition of the $CH_4/H_2/Ar$ gaseous mixtures influenced the signal positions and intensities. When the methane percentage was increased (solid to dashed line), the reduction process was extended to higher times or temperatures. Note that with both methane–gaseous mixtures, the carburization process at 7200 s and 1223 K was still incomplete due to a failure in the return of the TCD signal to the base line ($y=0$). With the green evaporated precursor, the reduction (Fig. 2b, dotted line) was registered at time or temperatures lower than those detailed for the precipitated precursor ($t < 2778$ s, $T < 760$ K). Besides, other signals were detected that included the pyrolysis of the metallic oxalates at $t < 1900$ s and $T < 605$ K. These features were also observed using the methane–gaseous mixture with the same hydrogen percentage (Fig. 2b, dashed line), followed by various positive and negative signals assigned to the solid-methane interaction. By increasing the hydrogen proportion with respect to methane (Fig. 2b, solid line), the TPRe profile was shifted to lower times or temperatures, a close return to the base line at $t=7200$ s, $T=1223$ K being noticed. Only negative signals dominated the fluffy black evaporated precursor TPRe profile in H_2/Ar (Fig. 2c) as a result of the gases production caused by the pyrolysis and carbothermal reduction of the precursor. This TCD signal could be described as the sum of the individual contributions of iron and niobium compounds prepared separately (see Supplementary data, Fig. Sd1). The termination of the process occurred at $t=6000$ s and $T=1223$ K.

Then, taking into account the evolution of the TPRe profiles, it can be inferred that (i) the $CH_4/H_2/Ar$ mixture 4/16/80 vol% in composition completes the carburization with the green evaporated precursor; while (ii) a mixture without methane is enough to arrive at a similar result with the fluffy-black-evaporated precursor. These observations are valid for a maximum mass of the solid precursors of 150–200 mg, subjected to a TPRe treatment up to 7200 s and 1223 K.

Fig. 3A and B shows the diffraction patterns from the brown precipitated precursor and from the green evaporated precursor after the temperature-programmed reaction with the different mixtures of $CH_4/H_2/Ar$, after 5600 s ($T=1223$ K). Under H_2/Ar flow, the brown precipitated precursor (Fig. 3A (a)) was reduced to $FeNb_2O_6$ (JCPDS card No. 34-0426), $Fe_4Nb_2O_6$ (JCPDS card No. 34-0433) and Fe (JCPDS card No. 06-0696). By incorporating methane to either of the two gas mixtures used (Fig. 3A (b–c)), compounds NbO_2 (JCPDS card No. 44-1053) and Fe were increasingly identified together with the $FeNb_2O_6$ oxide. This phase evolution would be consistent with the $NiNb_2O_6$ reduction proposed by Pereira et al. [15] according to the following reaction:

$$NiNb_2O_6 + 2H_2 \rightarrow Ni + 2NbO_2 + 2H_2O$$

Consequently, under these conditions methane would only increase the reducing character of the mixture promoting the progressive reduction of $FeNb_2O_6$ into NbO_2 and Fe. So far,

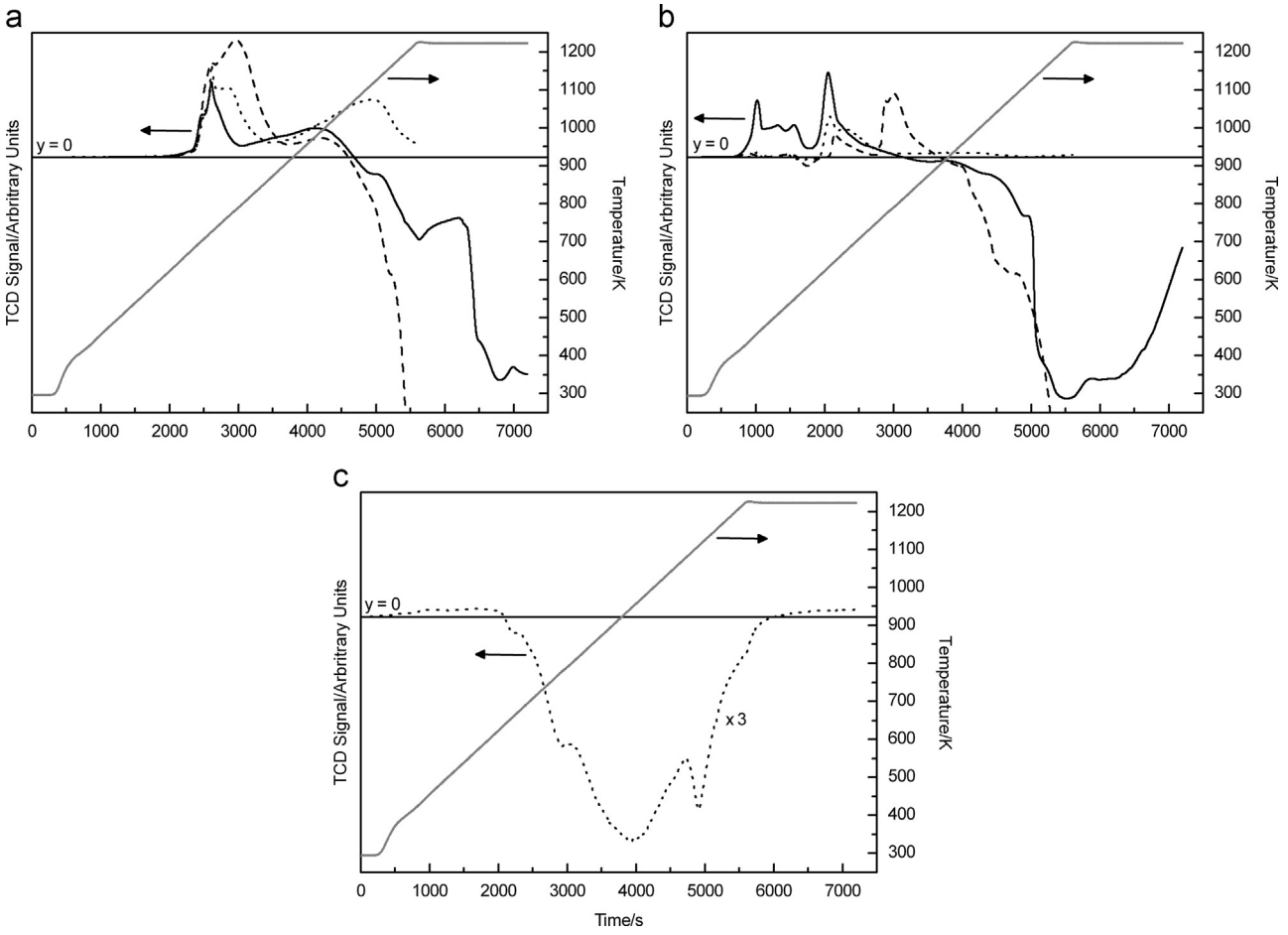

Fig. 2. Temperature-programmed reaction profiles of (a) brown precipitated, (b) green evaporated and (c) fluffy black evaporated precursors in different $CH_4/H_2/Ar$ gas mixtures:· dotted line 0/4/96 vol%, dashed line 16/4/80 vol% and solid line 4/16/80 vol%. The gray line corresponds to the heating sequence up to 7200 s and 1223 K.

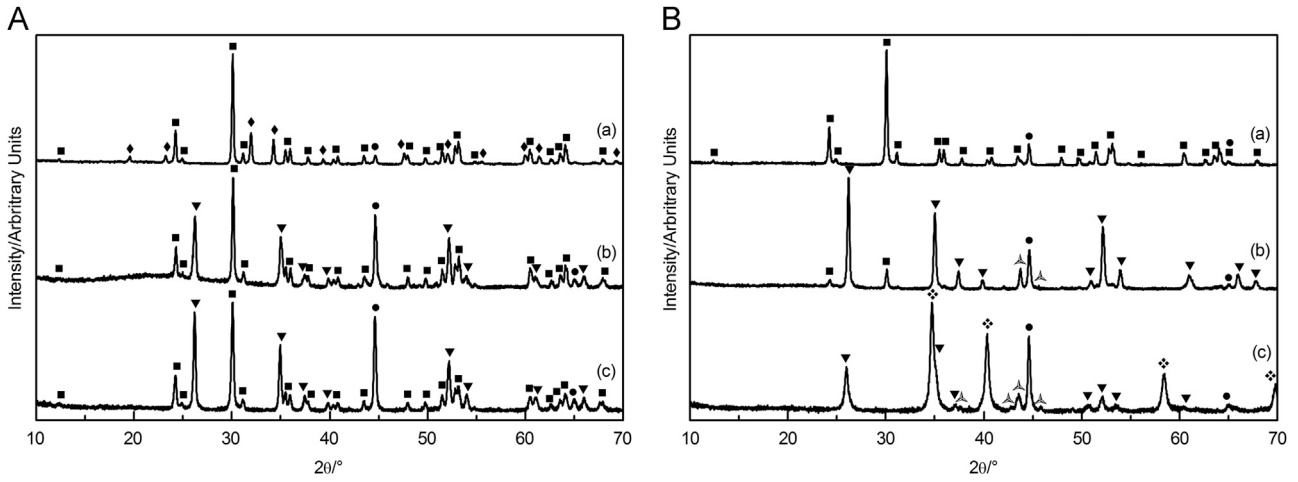

Fig. 3. X-ray diffraction patterns of the products obtained after the temperature-programmed reaction from **A** brown precipitated and **B** green evaporated precursors in different $CH_4/H_2/Ar$ gas mixtures: (a) 0/4/96 vol%, (b) 16/4/80 vol% and (c) 4/16/80 vol%, stopped at 5600 s ($T = 1223$ K). Marked reflections correspond to: ■ $FeNb_2O_6$ (JCPDS card No. 34-0426), ◆ $Fe_4Nb_2O_6$ (JCPDS card No. 34-0433), ● Fe (JCPDS card No. 06-0696), ▾ NbO_2 (JCPDS card No. 44-1053), ❖ NbC (JCPDS card No. 38-1364), ⅄ Fe_3C (JCPDS card No. 34-0001/35-0772).

the absence of niobium carbide has confirmed the previous analysis of the TPRe profiles (Fig. 2a, solid and dashed lines). With the green evaporated precursor, the reduction products in H_2/Ar were $FeNb_2O_6$ and Fe (Fig. 3B (a)). From the interaction with the high-content mixture, a greater conversion of $FeNb_2O_6$ to NbO_2 and Fe was noticed with respect to that of

the precipitated precursor, with the additional formation of Fe_3C (JCPDS card No. 34-0001/35-0772) (Fig. 3B (b)). On the other hand, by decreasing the methane percentage NbC did form (JCPDS card No. 38-1364), the amount of NbO_2 decreased, and the proportion of Fe and Fe_3C (Fig. 3B (c)) increased. Therefore, this precursor would be more reactive than the precipitated precursor to the reduction–carburization process, thus again confirming what was evidenced by the TPRe profiles. This increase could be attributed to the additional supply of carbon in the precursor solid phase, coming from the pyrolysis of metallic oxalates in reducing atmosphere.

In the case of the fluffy black evaporated precursor, a carbothermal reduction in H_2/Ar was detected. The Fe–NbC/C composite appeared together with Fe_3C, which is consistent with the return of the TCD signal to the base line (see Supplementary data, Fig. Sd2). For the sake of comparison, Fig. 4 shows the diffraction patterns corresponding to different precursors prepared after the TPRe reaction in the gaseous mixtures which yielded a higher conversion to NbC (4/16/80 and 0/4/96 vol% CH_4/H_2/Ar) after a time longer than 9000 s ($T=1223$ K). The Fe–NbC composite was formed in all combinations; a still incomplete reaction was noticed with the precipitated precursor (Fig. 4a) and a complete reaction with the two remaining evaporated precursors (Fig. 4b and c). When this type of precursors was used, the 002 Bragg diffraction, typical of carbon at $2\theta \sim 26^\circ$, was registered. The presence of Fe_3C indicated the reaction between the iron particles and the carbon from either the gas phase (Fig. 4a) or the solid phase (Fig. 4c), or a combination of both phases (Fig. 4b). The size of the niobium carbide crystallite was 67 nm for the green evaporated precursor and 12 nm for the fluffy black evaporated precursor (Fig. 4b and c). This considerable difference, associated with the precursor origins, was not observed in the Fe metallic phase, whose crystallite size remained close to 60 nm.

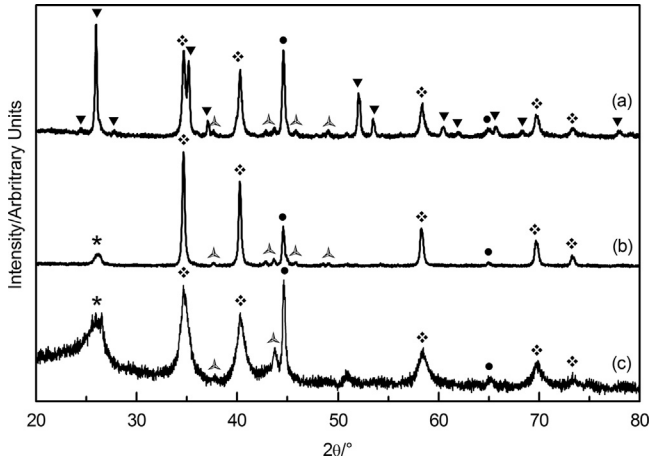

Fig. 4. X-ray diffraction patterns of the products obtained after the temperature-programmed reaction from (a) brown precipitated in 4/16/80 vol% CH_4/H_2/Ar, (b) green evaporated in 4/16/80 vol% CH_4/H_2/Ar and (c) fluffy black evaporated in 0/4/96 vol% CH_4/H_2/Ar precursors, stopped at 9000 s ($T=1223$ K). Marked reflections correspond to: ▾ NbO_2 (JCPDS card No. 44-1053), ❖ NbC (JCPDS card No. 38-1364), ⅄ Fe_3C (JCPDS card No. 34-0001/35-0772), ● Fe (JCPDS card No. 06-0696), * C (JCPDS card No. 41-1487).

3.2. Carbon analysis and microstructure of Fe–NbC/C composite powders

The total carbon content of the compound powders in Fig. 4b and c, derived from the green evaporated precursor and from the fluffy black evaporated precursor, was 40 and 70 wt%, respectively. These values, well above the theoretical percentage for the Fe–NbC composition showed the formation of a carbon-based compound material. Fig. 5 shows the LR spectra corresponding to two broad bands denominated D (Disordered) at $\sim 1350\ cm^{-1}$ and G (Graphitic) at $\sim 1580\ cm^{-1}$, which typically exhibit the disordered carbons [16,17]. In both registers, a smaller peak could be observed associated with the D band in $\sim 1450\ cm^{-1}$, which was reported in hydrogenated amorphous carbon films (a-C:H) [18]. The predominance of mode D over G, both in the carbon derived from oxalate pyrolysis and possibly from the methane cracking (green evaporated precursor, Fig. 5a) and in the one generated by PVA–sucrose pyrolysis (fluffy black evaporated precursor, Fig. 5b), reflects a high degree of disorder in the carbon present in the compound powders, of nanometric dimensions.

Based on these results, it is possible to interpret the differences found in the NbC crystallite size determined by XRD for the powders from the different evaporated precursors. A high content of nanometric amorphous carbon, similar to the one that is achieved with the fluffy black evaporated precursor, would be acting as dispersing phase, thus limiting the growth of NbC particles but not the growth of Fe particles. Consequently, the incidence of the carbon source over the mechanism of the reinforcing phase formation (NbC) of the compound material should be remarked.

Fig. 6 shows the typical morphology of Fe–NbC/C composite powders, again reflecting the dependence on the precursor origin and, hence, on the amount and type of carbon source used. At low magnification, irregular aggregates were identified of similar external shape and a mean size of 100–130 μm (Fig. 6a, c and e). The same aggregates were more clearly distinguished in surface and internal morphology at high magnification

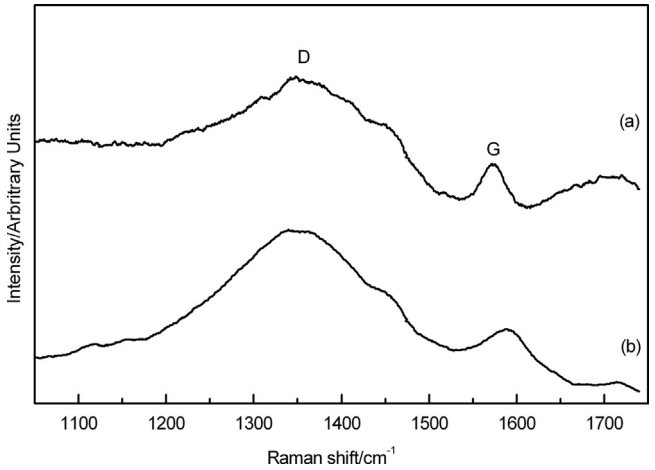

Fig. 5. Laser Raman spectra of the products obtained after the temperature-programmed reaction from (a) green evaporated in 4/16/80 vol% CH_4/H_2/Ar and (b) fluffy black evaporated in 0/4/96 vol% CH_4/H_2/Ar precursors, stopped at 9000 s ($T=1223$ K).

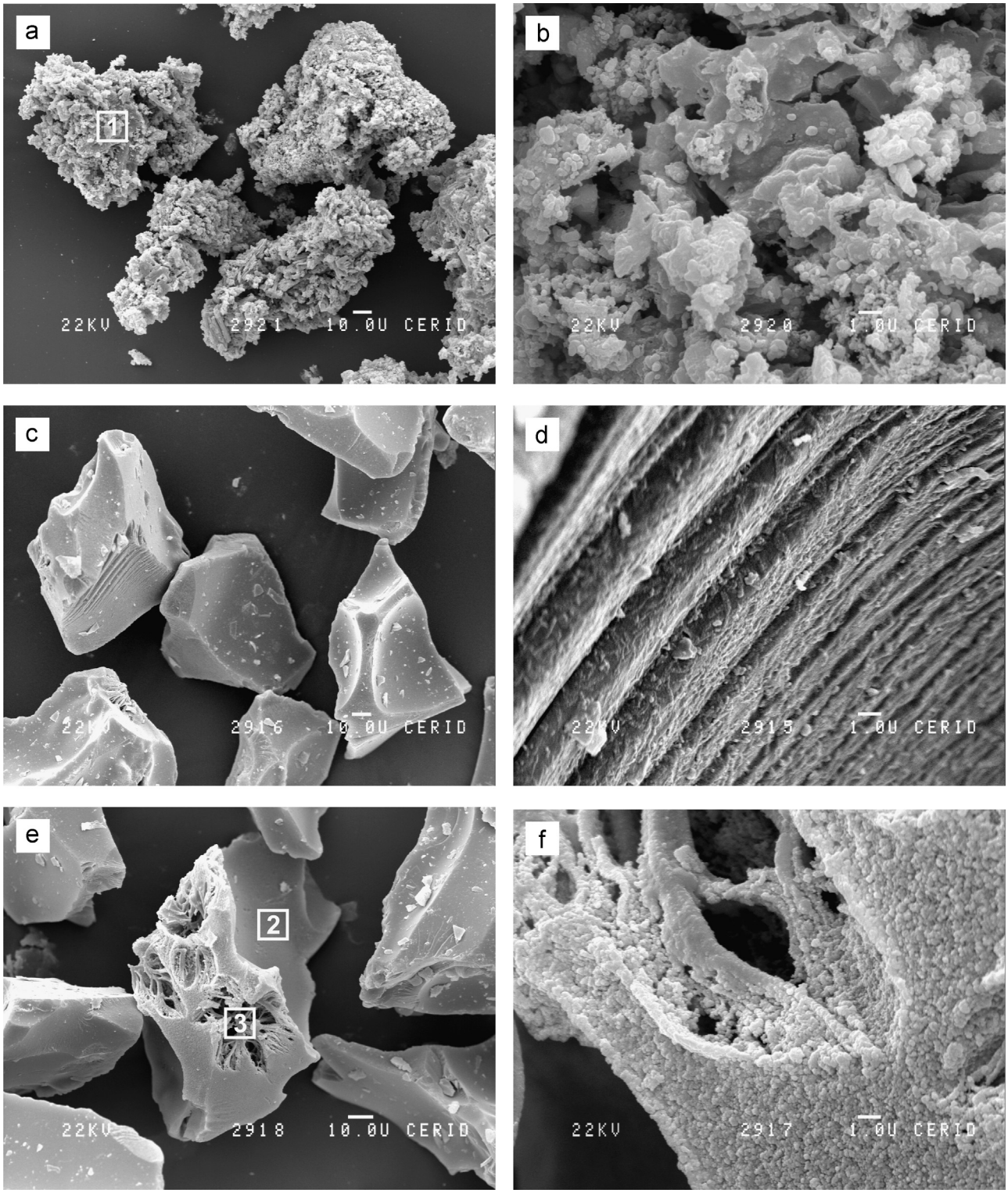

Fig. 6. Scanning electron microscopy images of the products obtained after the temperature-programmed reaction from (a, b) green evaporated in 4/16/80 vol% $CH_4/H_2/Ar$ and (c–f) fluffy black evaporated in 0/4/96 vol% $CH_4/H_2/Ar$ precursors, stopped at 9000 s ($T = 1223$ K).

(Fig. 6b, d and f). From the green evaporated precursor, the more compact agglomerates presented a granular substructure of rounded units close to 1 μm (Fig. 6a and b). Instead, when the fluffy black evaporated precursor was used, layers or strata, concave cavities and a porous internal structure could be observed (Fig. 6c, d and e). The high-magnification view of that internal structure (Fig. 6f) revealed rounded subunits of a uniform size close to 0.25 μm which formed a fibrous network.

Since metal iron is known to be dissolved in a HCl solution, the separation of NbC/C from the composite powders was

conducted by leaching with dilute HCl at 60 °C for 24 h. After removing the iron in solution by successive washing with demineralized water, the powders were dried and analyzed again by XRD and SEM (see Supplementary data, Fig. Sd3–Sd4). Comparing these results with those presented in Figs. 4b, c and 6a, e both the disappearance of the diffraction peaks assigned to metal iron and the morphology described before were confirmed. Details of acid erosion became visible only at high magnification, suggesting a different iron distribution in relation to the starting precursor evaporated (green or fluffy black).

Fig. 7 shows the results of microanalysis corresponding to the marked zones 1, 2 and 3 in the SEM micrographs (Figs. 6a, c and Sd4a, c), before (A) and after (B) the procedure of attack acid. A Fe:Nb molar relation close to the nominal composition (Fe:Nb = 1:1) was determined in using the green evaporated precursor (Fig. 7A (a)), noticing slight deviations between the different aggregates analyzed. This trend was also verified by preparing the same type of precursor from a Fe:Nb = 0.5:1 source solution (see Supplementary data, Fig. Sd5–Sd7) and on similar aggregates subsequently leached in dilute hydrochloric acid (Fe:Nb ≤ 0.1:1, Fig. 7B(a). In the case of the fluffy black evaporated precursor, the concave cavities were mostly composed of Nb, whose composition was not altered by the acid treatment (Fig. 7b, A and B) whereas the internal porous structures had Fe as major metal that was evidently dissolved by hydrochloric acid (Fig. 7c, A and B). Once more the molar ratio Fe:Nb was reduced to 0.1:1, now exposing the Nb element. Both the concave surfaces and the internal structure here characterized would be related to the precursor pyrolysis defined by the behavior of PVA and sucrose in acid metallic solutions [19].

3.3. Oxidation behavior of Fe–NbC/C composite powders

Fig. 8 shows typical TGA/DTA profiles of the Fe–NbC/C composite particles studied at temperatures below 1000 °C in flowing air. From the TGA curves (solid line), it can be observed that the weight percentage of the samples does not change significantly below ~600 K. A slight weight loss (5%) can be observed only when using the fluffy black evaporated precursor associated with water endothermal desorption at 338 K (Fig. 8b, dashed line DTA-curve). This difference with respect to the green evaporated precursor (Fig. 8a) is probably due to the distinct spongy microstructure described for the composite prepared with PVA–sucrose.

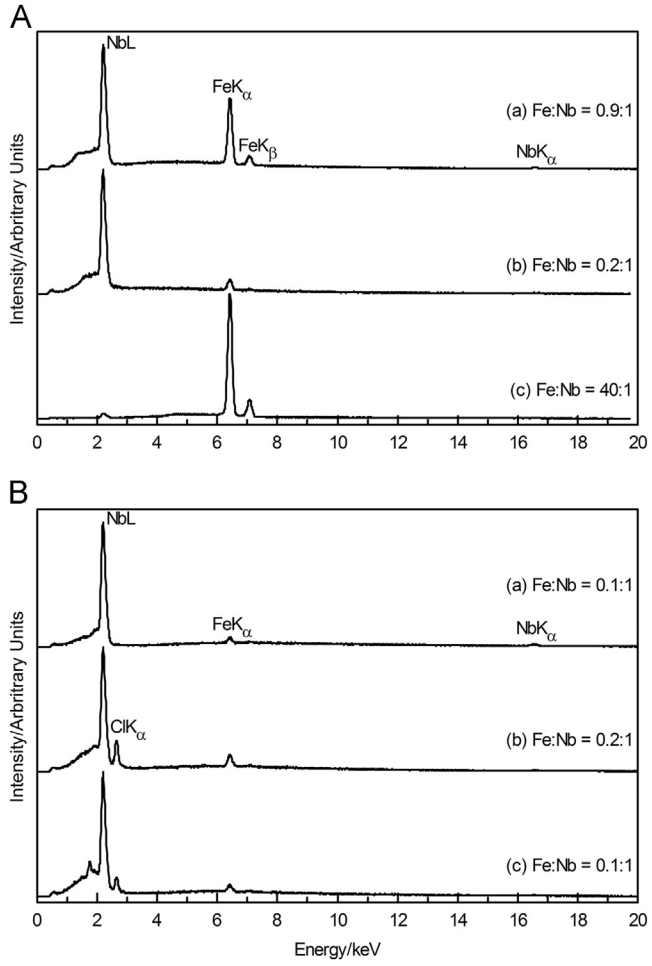

Fig. 7. Energy-dispersive X-Ray Spectroscopy patterns corresponding to zones marked 1 (a), 2 (b) and 3 (c) in SEM micrographs (Fig. 6a, e and Fig. Sd4a, c), before (A) and after (B) dissolving metal iron from composite powders.

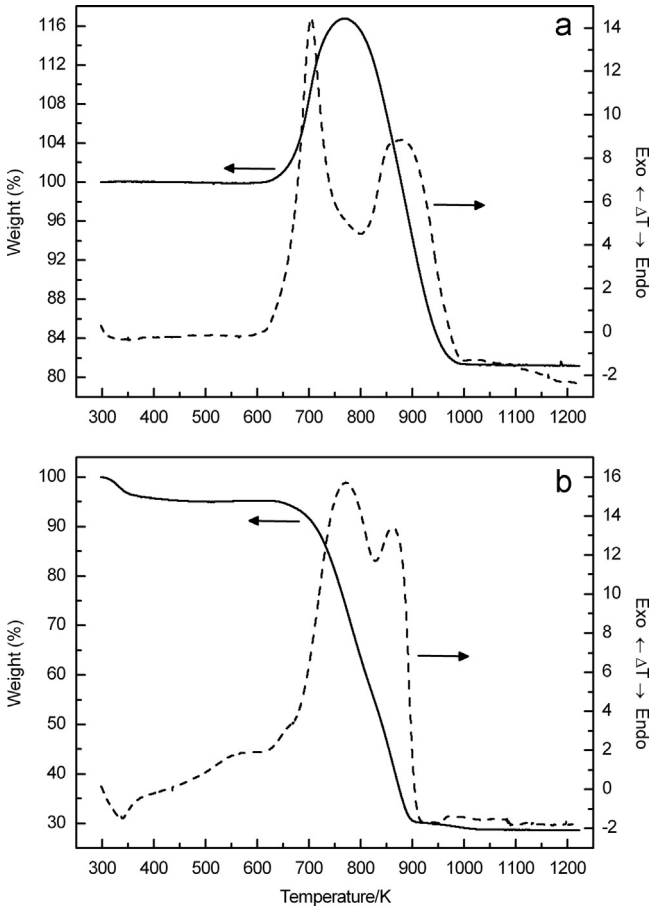

Fig. 8. Thermogravimetric and differential thermal profiles in air of the products obtained after the temperature-programmed reaction from (a) green evaporated in 4/16/80 vol% $CH_4/H_2/Ar$ and (b) fluffy black evaporated in 0/4/96 vol% $CH_4/H_2/Ar$ precursors, stopped at 9000 s ($T = 1223$ K).

The onset of the oxidation of both composite powders is found to start at about 600 K and extend up to 1040 K. The differences registered in the TGA/DTA profiles in the 600–1040 K temperature range can be interpreted by essentially taking into account total carbon analysis. In the case of Fig. 8a (sample with 40 wt% carbon), the mass gain observed up to 770 K could be due to the oxidation of Fe/Fe_3C and NbC. However, when comparing the exothermal DTA peak at 700 K with literature data, it is possible to assign this first event to the oxidation of Fe/Fe_3C [20,21]. On the other hand, the loss of net mass registered at temperatures higher than 770 K and the corresponding exothermal DTA peak at 880 K probably include the NbC oxidation [22,23] together with free carbon [24]. In turn, in Fig. 8b, the TGA profile is dominated only by a mass loss in the 600–1040 K range, due to the high carbon content (70 wt%). That profile is analogous to the one reported by Rufino et al. [24] for carbide-derived carbon on β-SiC nanoparticles by reaction with chlorine. From the comparison of Fig. 8b with the TGA/DTA curves of the NbC/C compound powder (see Supplementary data, Fig. Sd8), it can be inferred that niobium carbide participates in the first exothermal peak while metallic iron and cementite participate in the second peak. The higher oxidation temperature proposed for the Fe/Fe_3C combination with respect to Fig. 8a could be explained in terms of a protecting effect of the carbon matrix generated by PVA–sucrose pyrolysis and NbC according to XRD/LRS/SEM-EDS results (Figs. 4c, 5b, 6e and 7b, c, A and B). Other reports supporting this hypothesis were also published by Cheng et al. [20] when they studied the Fe resistance to the oxidation of particles made up of Fe(core)/SiO_2(shell). These authors found a shift in the order of 100 K in the TGA/DTA changes when protecting iron nanoparticles with a silica layer.

Finally, above 1040 K, the weight percentage remains almost constant. The ternary oxide $FeNbO_4$ (JCPDS card No. 16-0374) is identified by XRD analysis as the major oxidation product finishing all the experiments.

4. Conclusions

Fe–NbC/C composite powders were synthesized using an *in situ* technique, which combines solution-derived precursors and a gas reduction–carburization reaction. The precursor type (with or without carbon) and the CH_4/H_2 ratio present in the gaseous mixture conditioned the end of the transformation at a given temperature. When the carbon was supplied by the gas phase (CH_4), the reaction mechanism proposed proceeded according to the following sequence:

$$FeNb_2O_6 \rightarrow Fe + NbO_2 \rightarrow Fe + NbC$$

In this case, the shorter reaction time was achieved by including carbon in the precursor formulation and using a gaseous mixture with a reducing rather than a carburizing character. When methane was replaced by carbon in the solid phase, from the PVA–sucrose pyrolysis, the transformation to the compound powder was achieved faster by means of a carbothermal reduction reaction.

The type of free carbon formed was characterized by a high degree of disorder and defined not only the powder microstructure but also the crystallite size of the reinforcement phase and certain behavior features during oxidation. The carbon generated by PVA–sucrose pyrolysis was the most adequate one to obtain a sponge-type morphology with nanocrystalline NbC (12 nm) and protect the Fe particles from oxidation.

It is expected that the compound powders thus obtained have a better consolidation performance, being of promissory interest for electrochemical applications (porous electrodes). The PVA–sucrose route is also presented as a new alternative for the production of nanocrystalline NbC/C powders.

Acknowledgments

This work was supported by projects C.A.I.+D. 2005/2009, No. 007-038/PE-358 of Universidad Nacional del Litoral, Argentina. The authors are also grateful to Companhia Brasileira de Metalurgia e Mineração, Araxa, Brazil, for kindly offering the niobium reagent. They are also grateful to the National Catalysis Center (CENACA-UNL), Argentina, for the use of its temperature-programmed reaction, X-ray diffraction and laser Raman spectroscopy facilities. Thanks are given to Nora Pratta for the SEM analyses and to Elsa Grimaldi for the English language editing.

Appendix A. Supplementary materials

Supplementary data associated with this article can be found in the online version at http://dx.doi.org/10.1016/j.ceramint.2014.06.083.

References

[1] E. Gordo, B. Gómez, R. González, E.M. Ruiz-Navas, Study for the development of Fe–NbC composites by advanced PM techniques, Mater. Sci. Forum 534–536 (2007) 637–640.
[2] A.E. Martinelli, D.S.A. Paulo, R.M. Nascimento, M.P. Tavora, U.U. Gomes, C. Alves, Dilatometric behavior and microstructure of sintered Fe–NbC and Fe–TaC composites, J. Mater. Sci. 42 (2007) 314–319.
[3] A.N. Klein, A.E. Martinelli, R.M. Nascimento, D.S.A. Paulo, B.C. de Freitas Guedes, C. Alves Jr., Microstructural characterization of conventionally and plasma-sintered Fe–NbC and Fe–TaC composites, Int. J. Powder Met. 47 (2011) 29–37.
[4] B.S. Terry, D.C. Azubike, A. Chryanthou, Carbothermic reduction as a potential means for the direct production of Fe–WC and Fe–NbC, NbC metal–matrix composites, J. Mater. Sci. 29 (1994) 4300–4305.
[5] N.T. Mudzanapabwe, O.S. Chinyamakobvu, D.J. Simbi, In situ carbothermic reduction of a ferro-columbite concentrate in the recovery of Nb and Ta as metal matrix composite from tin smelting slag waste dump, Mater. Des. 25 (2004) 297–302.
[6] P.G. Esteban, E. Gordo, Development of Fe–NbC cernet from powder obtained by self-propagating high temperature synthesis, Powder Metall. 49 (2006) 153–159.
[7] L. Zhong, Y. Xu, X. Liu, F. Ye, Study on NbC particulate-reinforced iron matrix composite produced in situ, J. Mater Sci. 46 (2011) 2814–2819.

[8] J. Kano, N. Sato, S. Suzuki, F. Saito, H. Suginobe, T. Shiokawa, Synthesis of niobium carbides from ferroniobium by mechanochemical method, ISIJ Int. 49 (2009) 458–462.
[9] S. Rasib, H. Zuhailawati, Effect of milling speed on properties of Fe–NbC composite prepared by mechanical alloying, Key Eng. Mater. 471–472 (2011) 804–808.
[10] S. Rasib, H. Zuhailawati, Mechanical alloying of Fe–Nb–N with different bail to powder weight ratio for the formation of Fe–NbC composite, Adv. Mater. Res. 620 (2013) 94–98.
[11] K.A. Yazovskikh, S.F. Lomayeva, Mechanosynthesis of Fe–NbC nanocomposite, J. Alloys Compd. 586 (2014) 565–567.
[12] G.H. Lee, S. Kang, Sintering of nano-sized WC–Co powders produced by a gas reduction–carburization process, J. Alloys Compd. 419 (2006) 281–289.
[13] M.F. Zawrah, Synthesis and characterization of WC–Co nanocomposites by novel chemical method, Ceram. Int. 33 (2007) 155–161.
[14] D.M. Adams, J.B. Baynor, Advanced Practical Inorganic Chemistry, John Wiley & Sons Ltd, Londres, 1965.
[15] M.M. Pereira, E.B. Pereira, L.Y. Lau, M. Schmal, The nickel–niobia–silica interactions at low nickel contents, Catal. Today 57 (2000) 291–296.
[16] A.C. Ferrari, J. Robertson, Interpretation of Raman spectra of disordered and amorphous carbon, Phys. Rev. B 61 (2000) 14095–14107.
[17] S. Urbonaite, L. Hälldahl, G. Svensson, Raman spectroscopy studies of carbide derived carbons, Carbon 46 (2008) 1942–1947.
[18] J. Schwan, S. Ulrich, B. Batori, H. Ehrhardt, S.R.P. Silva, Raman spectroscopy on amorphous carbon films, J. Appl. Phys. 80 (1996) 129–281.
[19] R.N. Das, Nanocrystalline ceramics from sucrose process, Mater. Lett. 47 (2001) 344–350.
[20] J. Cheng, X. Ni, H. Zheng, B. Li, X. Zhang, D. Zhang, Preparation of Fe (core)/SiO_2 (shell) composite particles with improved oxidation-resistance, Mater. Res. Bull. 41 (2006) 1424–1429.
[21] N. Shpaisman, E.R. Bauminger, S. Margel, One-step synthesis of air-stable nanocrystalline iron particles by thermal decomposition of triiron dodecacarbonyl, J. Alloys Compd. 454 (2008) 89–96.
[22] J. Ma, M. Wu, Y. Du, S. Chen, W. Jin, L. Fu, Q. Yang, A. Wen, Formation of nanocrystalline niobium carbide (NbC) with a convenient route at low temperature, J. Alloys Compd. 475 (2009) 415–417.
[23] L. Shi, Y. Gu, L. Chen, Z. Yang, J. Ma, Y. Qian, Synthesis and oxidation behavior of nanocrystalline niobium carbide, Solid State Ionics 176 (2005) 841–843.
[24] B. Rufino, S. Mazerat, M. Couvrat, C. Lorrette, H. Maskrot, R. Pailler, The effect of particle size on the formation and structure of carbide-derived carbon on ß-SiC nanoparticles by reaction with chlorine, Carbon 49 (2011) 3073–3083.